

A Large Source of Cloud Condensation Nuclei from New Particle Formation in the Tropics

Christina J. Williamson^{1,2}, Agnieszka Kupc^{2,3}, Duncan Axisa^{4†}, Kelsey R. Billsback⁵, ThaoPaul Bui⁶, Pedro Campuzano-Jost^{1,7}, Maximilian Dollner³, Karl D. Froyd^{1,2}, Anna L. Hodshire⁵, Jose L. Jimenez^{1,7}, John K. Kodros^{5‡}, Gan Luo⁸, Daniel M. Murphy², Benjamin A. Nault^{1,7}, Eric A. Ray^{1,2}, Bernadett Weinzierl³, James C. Wilson⁴, Fangqun Yu⁸, Pengfei Yu^{1,2*}, Jeffrey R. Pierce⁵, Charles A. Brock²

1. Cooperative Institute for Research in Environmental Sciences, University of Colorado, Boulder, CO 80309, U.S.A.
2. Earth System Research Laboratory, National Oceanic and Atmospheric Administration, Boulder, CO 80305, U.S.A.
3. Faculty of Physics, Aerosol and Environmental Physics Group, University of Vienna, 1090 Vienna, Austria
4. Department of Mechanical and Materials Engineering, University of Denver, Denver, CO 80208, USA
5. Department of Atmospheric Science, Colorado State University, Fort Collins, CO 80523, USA
6. Earth Science Division, NASA Ames Research Center, Moffett Field, California, USA
7. Department of Chemistry, University of Colorado, Boulder, CO, USA
8. Atmospheric Sciences Research Center, State University of New York at Albany, Albany, New York, USA

Cloud condensation nuclei (CCN) can affect cloud properties and therefore the Earth's radiative balance^{1,2,3}. New particle formation (NPF) from condensable vapours in the free troposphere has been suggested to contribute to CCN, especially in remote, pristine atmospheric regions⁴, but direct evidence is sparse, and the magnitude of this contribution is uncertain^{5,6,7}. Here we use in-situ aircraft measurements of vertical profiles of aerosol size distributions to present a global-scale survey of NPF occurrence. We observed intense NPF occurring at high altitude in tropical convective regions over both the Pacific and Atlantic Oceans. Together with the results of chemical-transport models, our findings indicate that NPF persists at all longitudes as a global-scale band in the tropical upper troposphere, covering about 40% of the Earth's surface. Furthermore, we find that this NPF in the tropical upper troposphere is a globally important source of CCN in the lower troposphere, where they can affect cloud properties. Our findings suggest that the production of CCN, as these new particles descend towards the surface, is currently not adequately captured in global models, because they tend to underestimate both the magnitude of tropical upper tropospheric NPF and the subsequent growth to CCN sizes. This has potential implications for cloud albedo and the global radiative balance.

New particles form when condensing gases produce stable clusters with a diameter $>\sim 1.5$ nm⁸. Growth by condensation and coagulation may enable particles to reach diameters $>\sim 60$ nm where they can act as CCN. Atmospheric observations are required to guide the incorporation of NPF mechanisms into models⁹. Large numbers of small particles have previously been observed

Now at

[†]Droplet Measurement Technologies, Longmont, CO 80503, USA

[‡]Institute of Chemical Engineering Sciences, ICE/FORTH, Patras, Greece

* Institute for Environment and Climate Research, Jinan University, Guangzhou, China

at high altitude in the tropics^{10,11,12} because deep convective clouds loft condensable vapours and remove most larger particles that compete with NPF as sinks for these vapours¹³ (Fig. 1). Newly formed particles grow to CCN sizes in subsiding air outside of the convective clouds¹⁴.

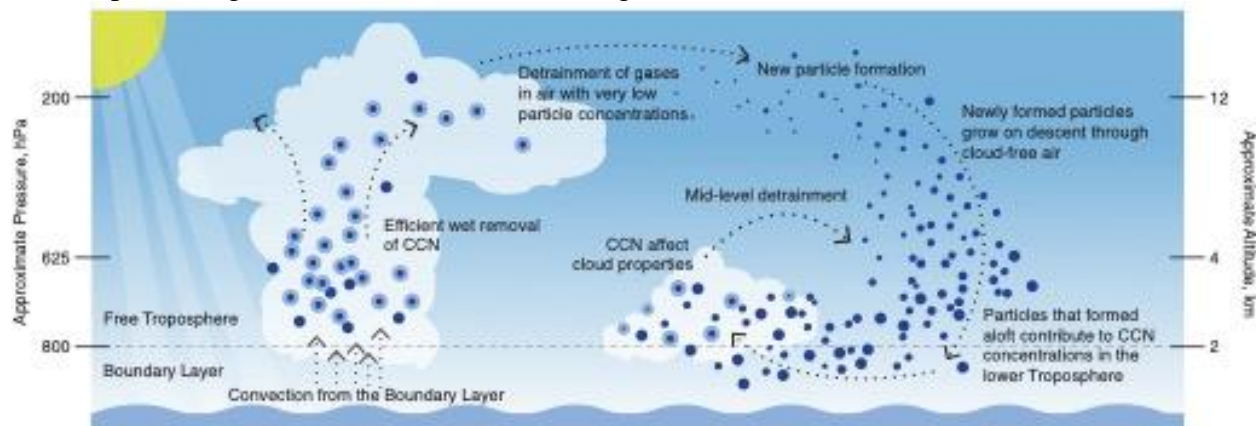


Figure 1 New particle formation and growth to CCN sizes in the tropical convective region. Left, deep convective clouds loft air from the boundary layer. Larger particles (CCN; dark blue circles) become activated to produce cloud droplets (light blue circles with dark centres) and are removed through precipitation and wet deposition ('wet removal'), reducing the condensation sinks that are found in air being moved from the cloud to the surrounding air ('detrained') at high altitude. Less-soluble aerosol precursors detrain, oxidize and form new particles, which grow by condensation and coagulation as they descend (right), with many reaching CCN sizes before they reach the top of the boundary layer. These CCN duly affect cloud properties. Image courtesy of K. Bogan, Cooperative Institute for Research in Environmental Sciences, University of Colorado, Boulder.

Global-scale measurements are needed to understand the scale and impact of NPF in the upper troposphere. Satellites cannot detect particles with diameters < 100 nm, and previous in-situ observations have been regional scale¹¹⁻¹³. We recently conducted in-situ, global-scale measurements of particle size distributions over the Pacific and Atlantic Oceans with near pole-to-pole coverage and systematic profiling between ~ 0.18 and ~ 12 km altitude over multiple seasons (Extended Data (ED) Fig. 1) on the NASA Atmospheric Tomography Mission (ATom)¹⁵. We observed evidence for abundant recent NPF at high altitudes within the tropical convective region (TCR, Figs. 2, 3 and ED Fig. 2) and subsequent particle growth during subsidence, and calculated the gas-phase condensation sink to all particles with diameters > 7 nm (CS_7) and the particle coagulation sink, which together govern the probability that particles will form and grow to reach CCN sizes (Methods). We observed this phenomenon in August and February, showing seasonal persistence.

In the TCR, high number concentrations occur over $\sim 30^\circ$ latitude over both Atlantic and Pacific Oceans (ED Fig. 2). NPF has also been observed at high altitude over the Amazon¹⁶. We compare our observations to four global-scale chemical-transport models with explicit size-resolved aerosol microphysics (ED Table 1). Some models that reproduce the observed pattern of small particles from NPF in the TCR indicate these particles persist as a nearly continuous band around the global tropics (ED Fig. 3). Together, these observations and models indicate that tropical NPF covers $\sim 40\%$ of the Earth's surface.

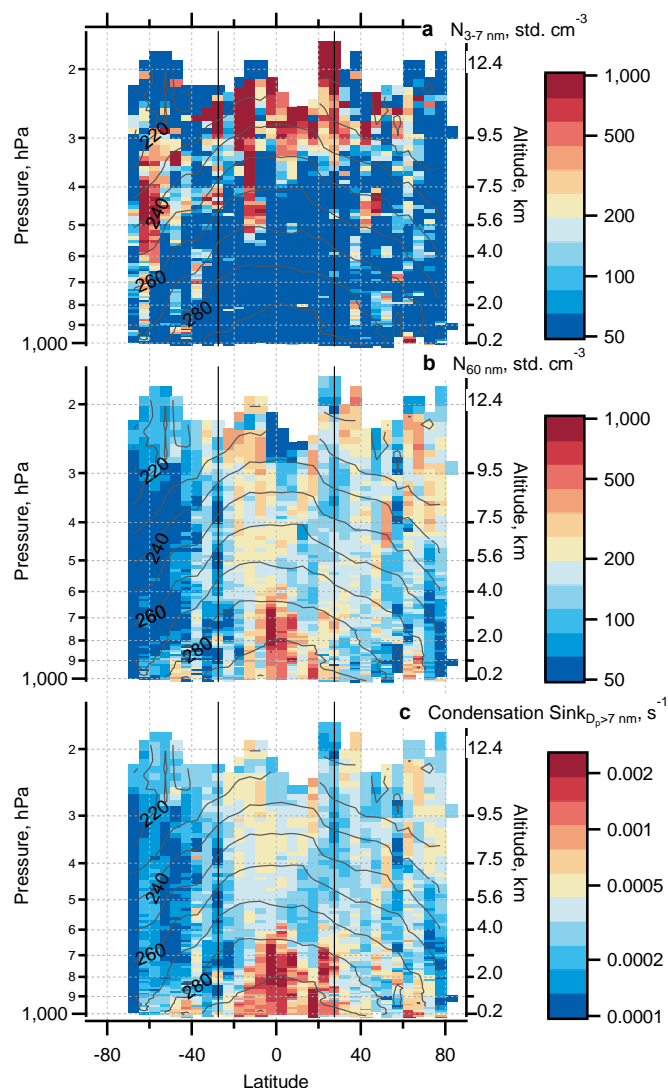


Figure 2 Average aerosol properties from ATom 1 and 2. *a*, Number concentrations of particles with diameters of between 3 nm and 7 nm, revealing high concentrations at high altitudes in the tropics. *b*, *c*, Average number concentration of particles bigger than 60 nm (*b*) and the condensation sink from all particles larger than 7 nm (*CS*₇; *c*), revealing mid to low values at high altitudes in the tropics. Grey curves show temperature contours (with 10 K spacing); black vertical lines show the latitude range of the TCRs. *std cm*⁻³, per cubic centimetre at standard temperature and pressure.

Deep convective clouds in the tropics enable NPF by removing pre-existing particles >60 nm, thus reducing sinks for small particles and condensable vapours^{13,17}. However, our measurements, which allow direct calculation of condensation and coagulation rates, show that tropical convection does not produce uniquely low sinks at high altitude in the TCR where the most recent NPF is observed (Fig. 2b, c; ED Fig. 4).

Therefore, further explanation is required for the consistently high numbers of particles from NPF observed in this region vs. others with even lower *CS*₇.

Low temperatures increase rates of NPF¹⁸. If condensable vapours were uniform across the atmosphere, we would expect to see the most particles produced by NPF at the lowest available temperatures and at the lowest *CS*₇. Globally, NPF occurs at temperatures <270 K and *CS*₇ <8 × 10⁻⁴ s⁻¹ (Figs. 2,3). Within the TCR, NPF occurs mainly at the lowest available *CS*₇ and temperature; however, in other regions of the troposphere much lower *CS*₇ and temperatures exist with weaker or no NPF. Therefore, a stronger source of condensable material must be available at high altitude in the TCR than in other cold, low-*CS*₇ areas (except in the Southern Ocean in February). This is likely due to a combination of convective activity in this region bringing precursor gases from lower altitudes (Fig. 1), and high solar elevation angles in the tropics increasing the hydroxyl radical (OH) availability to produce condensable vapours at faster rates¹⁹.

Within the TCR, median particle diameters increase fairly continuously with decreasing altitude (Fig. 4a). This indicates particle growth over time, since these data are from cloud-free air (Methods), which has a general descending motion²⁰ and remains mostly in the tropics (ED Fig. 5). The observed increase in particle size with decreasing altitude is inconsistent with mixing from continental boundary layer air, where size distributions instead show a substantial

accumulation (~60–500 nm) or nucleation (~2–12 nm) mode accompanying the Aitken (~12–60 nm) mode (ED Fig. 6b).

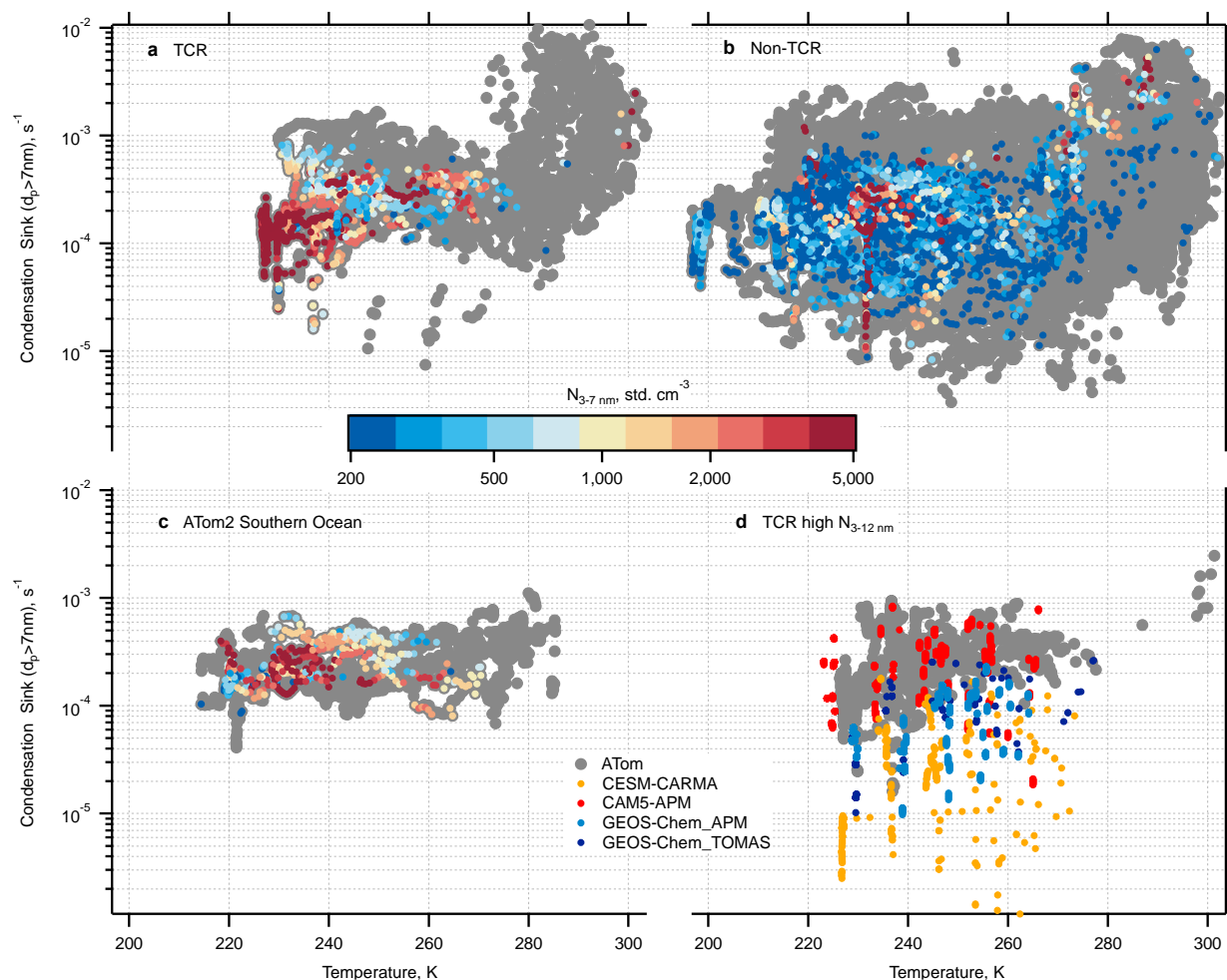


Figure 3 The relationship between CS7, temperature and NPF. a–c, Temperature and CS7 values for the TCR (a), non-TCR (b) and Southern Ocean in February (c), with colours showing statistically significant concentrations of particles with diameters of 3–7 nm (N_{3-7}) (see Methods for definition of ‘statistically significant concentrations’). Grey points indicate data for which concentrations of N_{3-7} were not statistically significant. Higher concentrations of 3–7-nm particles are observed for given temperatures and CS7 values within the TCR than elsewhere (except in the Southern Ocean during February), suggesting a greater availability of condensable vapours in the TCR. d, Observed (grey) and modelled (coloured) CS7 and temperature values in the TCR for number concentrations of 3–12-nm particles that exceeded $1,750 \text{ cm}^{-3}$. All models except CAM5-APM show high concentrations of 3–12-nm particles at lower CS7 values than observed.

High number concentrations of particles $>60 \text{ nm}$ (N_{60} ; large enough to act as CCN in convective clouds at $< 1\%$ supersaturation²¹) are seen in the lower troposphere (Fig 4c) (although N_{60} is fairly constant, the fraction of particles $> 60 \text{ nm}$ increases with decreasing altitude). Air at middle and lower altitudes in the TCR is a mix of descending air, which has reduced RH , and air from lower altitudes, as shown by higher measured RH (ED Fig. 7). However, concentrations of N_{60} increase with decreasing RH at mid-altitudes (Fig. 4d), indicating that CCN-sized particles are more abundant in the dry descending air than in the moist air from lower altitudes. 30–60 nm particles exist in the TCR marine boundary layer (MBL), but are unlikely to be primary^{22,23}. Lacking an evident source within the tropical MBL (no strong NPF events, Fig. 2a, and few

nucleation mode particles, ED Fig 6c), these particles may originate from the free troposphere. Previous studies have observed NPF at the top of the MBL^{24,25}, but we do not observe this within the TCR (although we observed it at other latitudes), and so conclude that this does not contribute significantly to particle concentrations here. Therefore, NPF at high altitude in the TCR appears to increase CCN concentrations in the lower troposphere, where they can affect cloud properties and thus the global radiation budget^{26,7}. Preliminary modeling studies suggest a global radiative effect of $\sim 0.1 \text{ W m}^{-2}$ from this CCN source (ED Fig. 10).

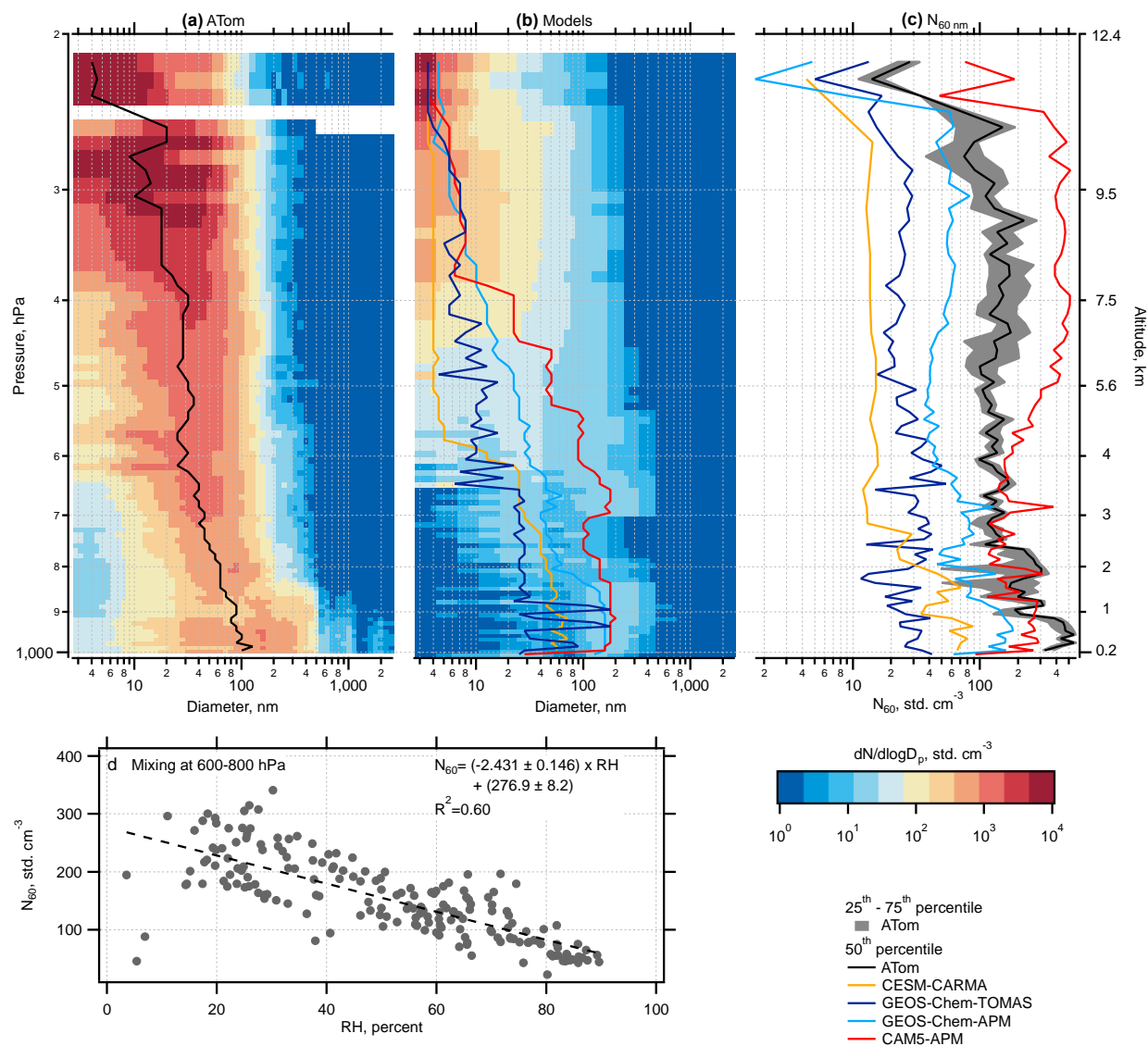


Figure 4 Evidence for particle growth on descent. All data are from the TCR. a, b, Average number size distribution as a function of pressure (having removed geographical regions with biomass burning and dust plumes), for ATom observations (a) and combined models (b). Mode diameters are shown with solid lines. D_p , particle diameter. c, Observed and modelled number concentrations of particles with diameters greater than 60 nm (N_{60}). d, Observed N_{60} values (grey data points) plotted against relative humidity at pressures of between 600 and 800 hPa, with a linear least-squares regression fit (dashed line). A relative humidity of more than 10% indicates mixing between descending and lower-altitude air. The increase in N_{60} values with decreasing relative humidity shows that descending air contains more CCN-sized particles than lower-altitude air.

Models show abundant NPF at high altitude in the TCR (although fewer nucleation mode particles are produced than in the observations), but, except for CAM5-APM (which significantly overestimates gas-phase volatile organic compounds at high altitude²⁷), produce much lower concentrations of CCN-sized particles than observed (Fig. 4b, c).

High-altitude TCR NPF occurs at higher CS_7 in the observations than in all models except CAM5-APM (Fig. 3d). Models produce fewer small particles at high altitude than observed (Fig. 4a, b; ED Fig. 7a). The overall performance of these models implies a deficit of condensable material and/or missing nucleation/growth mechanisms, especially because increasing CS_7 to match observations would reduce the modeled particle concentrations even further. Previous observations¹¹ also underestimated sinks in this region by considering only particles >60 nm, so the higher observed CS_7 values from ATom (Fig. 2b and 3a) represent a departure from the models and previous observations.

Sensitivity analysis (Methods, ED Fig. 10) shows that errors in nucleation rate or mechanisms are unlikely to cause the model underprediction of particle concentrations since substantial scaling of nucleation rates did not produce a substantial change in the particle size distribution and resulting number of CCN. This is due to a feedback whereby increasing nucleation rates slows growth rates and increases coagulation rates, thus dampening the sensitivity of CCN to changes in nucleation²⁸. Uncertainty in the amount of inorganic condensable material is also shown to have little effect on the result number of CCN.

Missing organics could also explain the underprediction. None of the models in this study include organic-mediated nucleation. Organics in the free troposphere are well known to be a dominant contributor to nanoparticle growth in the boundary layer and under many conditions²⁹, though they remain poorly simulated in many models³⁰. Organic matter significantly contributes to the mass of 50-500 nm particles at high altitudes in the TCR (ED Fig. 7). All models except CAM5-APM underestimate organic mass at high altitudes, suggesting they are missing organic species or growth mechanisms necessary to reproduce these observations.

The underprediction of N_{60} at lower altitudes suggests that models may scavenge growing particles too efficiently during their descent. Convective wet scavenging and aqueous processing in GEOS-Chem -TOMAS, -APM, and CAM5-APM affect all particles in a grid box, as particles in cloudy and clear portions mix at each time-step, whereas in reality the cloudy and clear regions do not generally mix quickly. This excess removal and processing of clear-sky aerosol by convective clouds in the models may cause the bimodal structure in the modeled mid- and lower- tropospheric size distributions (ED Fig. 6) that is caused by aqueous sulfate formation in activated aerosol in convective clouds, but which does not appear until lower altitudes in the observations.

Reducing cloud-processing on descent (a proxy for correcting the clear-sky removal of aerosol) allows modeled N_{60} and CS_7 to better represent ATom observations (Methods, ED Fig. 10). A full correction would need to track in-cloud particles between simulation time-steps. CESM-CARMA, which correctly accounts for sub-grid clear-sky and cloudy aerosol tracking, shows a larger increase in N_{60} with altitude than the other models (Fig. 4), indicating that this correction

may allow models with more complex nucleation schemes to capture the resultant increase in N_{60} observed on ATom.

It is therefore likely that many models may underestimate CCN in the remote tropical lower troposphere because they remove too many of the particles that form in the tropical upper troposphere through physically incorrect sub-grid aqueous aerosol processing and removal. Missing organics, or the mechanisms to include them in nucleation and growth may also be a factor. This is important for estimates of aerosol-cloud-radiation effects, as the radiative effect of NPF in the tropical upper troposphere could be on the order of 0.1 W m^{-2} globally (Methods, ED Fig. 10).

References

- 1 Rosenfeld, D., Sherwood, S., Wood, R. & Donner, L. Climate effects of aerosol-cloud interactions. *Science* **343**, 379-380, doi:10.1126/science.1247490 (2014).
- 2 Boucher, O. *et al.* in *Climate Change 2013: The physical science basis. Contribution of working group I to the Fifth assessment report of the intergovernmental panel on climate change* (eds T.F. Stocker *et al.*) Ch. 7, 571–658 (Cambridge University Press, 2013).
- 3 Dusek, U. *et al.* Size matters more than chemistry for cloud-nucleating ability of aerosol particles. *Science* **312**, 1375-1378, doi:10.1126/science.1125261 (2006).
- 4 Gordon, H. *et al.* Causes and importance of new particle formation in the present-day and preindustrial atmospheres. *J Geophys Res-Atmos* **122**, 8739-8760, doi:10.1002/2017jd026844 (2017).
- 5 Merikanto, J., Spracklen, D. V., Mann, G. W., Pickering, S. J. & Carslaw, K. S. Impact of nucleation on global CCN. *Atmos. Chem. Phys.* **9**, 8601-8616, doi:10.5194/acp-9-8601-2009 (2009).
- 6 Pierce, J. R. & Adams, P. J. Uncertainty in global CCN concentrations from uncertain aerosol nucleation and primary emission rates. *Atmos. Chem. Phys.* **9**, 1339-1356, doi:DOI 10.5194/acp-9-1339-2009 (2009).
- 7 Clarke, A. D. *et al.* Free troposphere as a major source of CCN for the equatorial pacific boundary layer: long-range transport and teleconnections. *Atmos. Chem. Phys.* **13**, 7511-7529, doi:10.5194/acp-13-7511-2013 (2013).
- 8 Kulmala, M. *et al.* Direct observations of atmospheric aerosol nucleation. *Science* **339**, 943-946, doi:10.1126/science.1227385 (2013).
- 9 Dunne, E. M. *et al.* Global atmospheric particle formation from CERN CLOUD measurements. *Science* **354**, 1119-1124, doi:10.1126/science.aaf2649 (2016).
- 10 Brock, C. A., Hamill, P., Wilson, J. C., Jonsson, H. H. & Chan, K. R. Particle formation in the upper tropical troposphere - a source of nuclei for the stratospheric aerosol. *Science* **270**, 1650-1653, doi:DOI 10.1126/science.270.5242.1650 (1995).
- 11 Clarke, A. D. *et al.* Nucleation in the equatorial free troposphere: Favorable environments during PEM-Tropics. *J. Geophys. Res. Atmos.* **104**, 5735-5744, doi:Doi 10.1029/98jd02303 (1999).
- 12 Weigel, R. *et al.* In situ observations of new particle formation in the tropical upper troposphere: the role of clouds and the nucleation mechanism. *Atmos. Chem. Phys.* **11**, 9983-10010, doi:10.5194/acp-11-9983-2011 (2011).

- 13 Clarke, A. D. *et al.* Particle production in the remote marine atmosphere: Cloud outflow and subsidence during ACE 1. *J. Geophys. Res. Atmos.* **103**, 16397-16409, doi:Doi 10.1029/97jd02987 (1998).
- 14 Clarke, A. D. & Kapustin, V. N. A Pacific aerosol survey. Part I: A decade of data on particle production, transport, evolution, and mixing in the troposphere. *J. Atmos. Sci.* **59**, 363-382, doi:Doi 10.1175/1520-0469 (2002).
- 15 Wofsy, S. C. *et al.* ATom: Merged Atmospheric Chemistry, Trace Gases, and Aerosols. ORNL DAAC, Oak Ridge, Tennessee, USA. <https://doi.org/10.3334/ORN LDAAC/1581> (2018).
- 16 Andreae, M. O. *et al.* Aerosol characteristics and particle production in the upper troposphere over the Amazon Basin. *Atmos. Chem. Phys.* **18**, 921-961, doi:10.5194/acp-18-921-2018 (2018).
- 17 Ekman, A. M. L., Wang, C., Strom, J. & Krejci, R. Explicit simulation of aerosol physics in a cloud-resolving model: aerosol transport and processing in the free troposphere. *J. Atmos. Sci.* **63**, 682-696, doi:Doi 10.1175/Jas3645.1 (2006).
- 18 Yue, G. K. & Hamill, P. Homogeneous nucleation rates of H₂SO₄-H₂O aerosol particles in air. *J. Aerosol Sci.* **10**, 609-614, doi:Doi 10.1016/0021-8502(79)90023-5 (1979).
- 19 Gao, R. S. *et al.* OH in the tropical upper troposphere and its relationships to solar radiation and reactive nitrogen. *J. Atmos. Chem.* **71**, 55-64, doi:10.1007/s10874-014-9280-2 (2014).
- 20 Folkins, I. & Martin, R. V. The vertical structure of tropical convection and its impact on the budgets of water vapor and ozone. *J. Atmos. Sci.* **62**, 1560-1573, doi:Doi 10.1175/Jas3407.1 (2005).
- 21 Fan, J. W. *et al.* Substantial convection and precipitation enhancements by ultrafine aerosol particles. *Science* **359**, 411-+, doi:10.1126/science.aan8461 (2018).
- 22 Raes, F., Entrainment of free tropospheric aerosols as a regulating mechanism for cloud condensation nuclei in the remote marine boundary layer. *J. Geophys. Res. Atmos.* **100**, 2893-2903, doi: 10.1029/94jd02832 (1995).
- 23 Quinn, P. K., Coffman, D. J., Johnson, J. E., Upchurch, L. M. & Bates, T. S. Small fraction of marine cloud condensation nuclei made up of sea spray aerosol. *Nat. Geosci.* **10**, 674-+, doi:10.1038/Ngeo3003 (2017).
- 24 Hegg, D. A., Radke, L. F. & Hobbs, P. V. Particle production associated with marine clouds. *J. Geophys. Res. Atmos.* **95**, 13917-13926, doi:DOI 10.1029/JD095iD09p13917 (1990).
- 25 Hoppel, W. A., Frick, G. M., Fitzgerald, J. & Larson, R. E. Marine boundary layer measurements of new particle formation and the effects nonprecipitating clouds have on aerosol-size distribution. *J. Geophys. Res. Atmos.* **99**, 14443-14459, doi:Doi 10.1029/94jd00797 (1994).
- 26 Kazil, J. *et al.* Modeling chemical and aerosol processes in the transition from closed to open cells during VOCALS-REx. *Atmos. Chem. Phys.* **11**, 7491-7514, doi:10.5194/acp-11-7491-2011 (2011).
- 27 Yu, F. A secondary organic aerosol formation model considering successive oxidation aging and kinetic condensation of organic compounds: global scale implications. *Atmos. Chem. Phys.* **11**, 1083-1099, doi:10.5194/acp-11-1083-2011 (2011).
- 28 Raes, F., VanDingenen, R., Cuevas, E., VanVelthoven, P. F. J. & Prospero, J. M. Observations of aerosols in the free troposphere and marine boundary layer of the

- subtropical Northeast Atlantic: Discussion of processes determining their size distribution. *J Geophys Res-Atmos* **102**, 21315-21328, doi:Doi 10.1029/97jd01122 (1997).
- 29 Trostl, J. *et al.* The role of low-volatility organic compounds in initial particle growth in the atmosphere. *Nature* **533**, 527-+, doi:10.1038/nature18271 (2016).
- 30 Tsigaridis, K. *et al.* The AeroCom evaluation and intercomparison of organic aerosol in global models. *Atmos. Chem. Phys.* **14**, 10845-10895, doi:10.5194/acp-14-10845-2014 (2014).

Acknowledgements: We thank J. Kazil, G. Feingold, T. Goren, D. Fahey and K. Aikin for contributions to this analysis, and the ATom leadership team, science team and crew for contributions to the ATom measurements.

Author contributions: CW, AK, CB, MD, BW, KF, DM, PCJ, BN, JJ collected the data, and CW wrote the manuscript with contributions from CB, AK, JP, KF, DM, PJ, JJ, and ER. CW, AK and CB analyzed the size distributions. MD and BW analyzed cloud properties. KF and DM analyzed single particle composition, and PCJ, BN, JJ analyzed bulk particle composition. JK, AH, KB, JP ran Geos-Chem-TOMAS and JP developed methods for understanding relevant tropical dynamics, GL and FY ran GEOS-Chem-APM and CAM5-APM, and PY ran CESM-CARMA. ER ran the ATom back-trajectories. DA and JW developed the relative differencing method.

Author Information: Reprints and permissions information is available at www.nature.com/reprints. The authors declare no competing interests. Readers are welcome to comment on the online version of the paper. Correspondence and requests for materials should be addressed to Williamson, C.J. (christina.williamson@noaa.gov).

Funding: The authors acknowledge support by the U.S. NASA's Earth System Science Pathfinder Program under award NNH15AB12I, NNX15AJ23G and NNX15AH33A, and by the U.S. National Oceanic and Atmospheric Administration (NOAA) Health of the Atmosphere and Atmospheric Chemistry, Carbon Cycle, and Climate Programs. AK is supported by the Austrian Science Fund's Erwin Schrodinger Fellowship J-3613. JP, JK, KB and AH were supported by the US Department of Energy's Atmospheric System Research, an Office of Science, Office of Biological and Environmental Research program, under grants DE-SC0019000 and DE-SC0011780; the U.S. National Science Foundation, Atmospheric Chemistry program, under grant AGS-1559607; and the NOAA, Office of Science, Office of Atmospheric Chemistry, Carbon Cycle, and Climate Program, under the cooperative agreement award NA17OAR430001. G.L. and F.Y. acknowledge funding support from NASA under grants NNX13AK20G and NSF under grant AGS-1550816. BW and MD have received funding from the European Research Council (ERC) under the European Union's Horizon 2020 research and innovation framework program under grant 640458 (A-LIFE) and from the University of Vienna.

Methods

Overview of the ATom mission.

Measurements were taken on the first two deployments of NASA's Atmospheric Tomography Mission (ATom; 29 July-23 August 2016 and 26 January-21 February 2017), referred to as ATom 1 and 2 respectively. This mission comprised four sets of contiguous flights over both Pacific and Atlantic Ocean basins from 81 °N to 65 °S. The flights focused on the remote marine atmosphere, constantly profiling between about 0.18 and 11-13 km altitude so as to resolve the vertical structure of the atmosphere (ED Fig. 1).

Summary of aerosol measurements.

Aerosol dry size distributions were measured from 2.7 nm – 4.8 µm diameter at 1 Hz time resolution with a suite of instrumentation³¹. Inside the DC-8, a Nucleation Mode Aerosol Size Spectrometer (NMASS), a custom-built battery of 5 condensation particle counters, each operated with different detection limits (d_{50}), provided 5 channels between 2.7 and 60 nm diameter³²⁻³⁴ on ATom 1. Two NMASSes were operated on ATom 2, providing 10 distinct channels over the same size-range. A commercial optical particle counter (OPC), the Ultra-High Sensitivity Aerosol Spectrometer (UHSAS, Droplet Measurement Technologies), specifically adapted to operate over rapidly changing pressures^{34,36}, measured from 60-500 nm. A second commercial OPC, Laser Aerosol Spectrometer (LAS, Thermo-Systems Engineering Co.) extended this distribution to 4.8 µm, which was the upper size limit at which particles could be efficiently sampled.

Dry (<40% RH) size distributions were measured at 1 Hz time resolution, which, given average aircraft ascent/descent rates of ~7 m/s, provides ~7 m vertical resolution in the atmosphere (with a range from ~ 11 m and the lowest altitudes to ~ 5 m at the highest). Fourier transform analysis of concentration measurements from the NMASS revealed statistical noise at frequencies >0.1 Hz³⁷ (ED Fig. 8), therefore we average the data to 0.1 Hz, giving average vertical resolution of 70 m (corresponding to 8 hPa at 1 km altitude and 3 hPa at 10 km altitude).

Cloud particle impaction on aircraft and inlet surfaces generates artifact particles that are then sampled by aerosol instruments³⁸. Therefore, all in-cloud size-distribution data were removed from the dataset before analysis. Clouds are identified by coarse mode number concentration measured with a second-generation Cloud, Aerosol, and Precipitation Spectrometer (CAPS, Droplet Measurement Technologies), temperature and relative humidity. Water, ice and mixed phase clouds were removed.

All concentrations are given at standard temperature and pressure (STP), 1013 hPa and 0 °C.

Identifying new particle formation.

To identify recent NPF, we identified times when the concentration in the smallest size channel of an NMASS ($d_{50} = 2.7$ nm) was significantly larger than that in the next-largest channel ($d_{50} = 6.9$ nm). Significantly larger means that the difference in concentrations was greater than could be expected from statistical variations in the sample (ED Fig. 9).

To identify statistically significant counts in the first channel, we assume that the counts in each channel can be described by Poisson statistics such that the variance in the number of counts, C_i , in a given channel, i , is given by

$$\text{Var}(C_i) = C_i. \quad (1)$$

The concentration measured in channel i , N_i , is

$$N_i = b_i C_i, \quad (2)$$

where b_i is a factor calculated from the flow rate, pressure and temperature corrections to STP and live-time correction.

Since variance follows the relationship

$$\text{Var}(aX) = a^2 \text{Var}(X), \quad (3)$$

we can describe the variance in the concentration in channel i as

$$\text{Var}(N_i) = b_i^2 \text{Var}(C_i) = b_i^2 C_i. \quad (4)$$

Because variance also follows the relationship

$$\text{Var}(X - Y) = \text{Var}(X) + \text{Var}(Y), \quad (5)$$

the standard deviation of the difference between concentrations in channels 1 and 2 in the NMASS is

$$\sigma_{diff} = \sqrt{b_1^2 C_1 + b_2^2 C_2}. \quad (6)$$

We consider that the difference between channel 1 and 2 is significant when

$$N_1 - N_2 > 3\sigma_{diff}. \quad (7)$$

For a 5° latitude by 10 hPa box for each ocean basin, we calculated the proportion of data points collected (at 0.1 Hz frequency) that show significant concentrations of small particles using Eq. 7.

Sink Calculations.

For each point in flight the condensation kernel for a sulfuric acid molecule with particles of each diameter in the size distribution, at the ambient temperature and pressure, is calculated using the Fuchs expression for coagulation rate coefficient³⁹, substituting a sulfuric acid molecule for one of the particles to get a condensation sink instead of a coagulation sink (and noting that the accommodation coefficient, α , in equation 12.57 p 664 in Seinfeld and Pandis³⁹ should read $1/\alpha$). We calculate the diameter of a sulfuric acid molecule from bulk properties following the method from Lovejoy et al.⁴⁰, neglecting temperature effects on the probability distribution function of monomers, dimers and trimers. Over the measurement conditions, this gives a diameter ranging between 0.545 and 0.552 nm. We take the mass of the sulfuric acid molecule to be 98.079 g/mol⁴¹. We assume each particle to have the density of water (1 kg m⁻³).

This is then multiplied by the number of particles in that size bin and summed over all bins to produce the condensation sink. Coagulation sinks are calculated in the same manner.

The condensation sink from particles >7 nm is correlated with coagulation sinks for particles of various sizes and the total surface areas (ED Fig. 4). Therefore, it is reasonable to assume that the relationships explored between new particle formation, condensation sinks and temperatures in the manuscript also hold for coagulation sinks.

Nucleation and growth rates are not sufficiently constrained by our data to calculate survival probabilities (probability of a particle of a given size surviving to reach CCN-sizes, these typically range from ~ 0.1 to 1 depending on the environment⁴²), but these calculated sinks allow

us to place our observations within the context of other studies of NPF and growth to CCN sizes. The condensation sink rate constant in the tropics above 700 hPa is generally below 0.0005 s^{-1} (Fig. 2c). The condensation rate is effectively the coagulation rate of a 'particle' the size of a molecule. The coagulation rate scales with $1/D_p$ of the smaller molecule/particle³⁹, where D_p is the particle diameter, so the coagulation loss rate for a 3 nm particle here would be 0.0001 s^{-1} . Coagulation rates tend to decrease with particle size, and so will be smaller as the particles grow through larger sizes and into the accumulation mode. Sources of condensable vapours may be lower in the remote upper troposphere than in the continental boundary layer, so we expect growth rates to be slower here, but condensation and coagulation sinks will also be much lower because fewer sources exist and deep convective clouds remove many of the larger particles, so loss rates are also lower than expected in the continental boundary layer.

Back-trajectories.

10 day back trajectories were calculated with the Bowman trajectory model⁴³ and NCEP GFS meteorology⁴⁴. Trajectories were initialized each minute along all of the ATom flight tracks. A cluster of 240 trajectories offset slightly both horizontally and vertically from the flight track locations were initialized each minute as an estimate of the trajectory uncertainties. The cloud fractions were based on satellite derived clouds⁴⁵ within 5 degrees longitude of the flight tracks averaged within 5-degree latitude bins.

Particle composition.

The Particle Analysis by Laser Mass Spectrometry (PALMS) instrument measures the size and chemical composition of individual aerosol particles with diameters from 150 – 4000 nm⁴⁶. Mass spectral signatures differentiate each particle into a compositional class such as biomass burning, mineral dust, sea salt, sulfate/organic/nitrate mixtures, and others. The number fraction of each particle class averaged over 1-3 minutes is indicative of relative abundance. Biomass burning fractions measure the influence of smoke on the aerosol population. Likewise, mineral dust fractions are used to identify dust plumes such as those from the Saharan desert. We removed data in the TCR prior to indicated analyses where biomass burning and dust particle types accounted for >40% and 10% of total particle number concentration respectively, to exclude plumes. For analysis of organic and sulfate mass, the PALMS size range was restricted to particles $\leq 500 \text{ nm}$.

A highly customized high-resolution time of flight aerosol mass spectrometer (HR-ToF-AMS, Aerodyne Research Inc.)⁴⁷⁻⁴⁹ measured non-refractory submicron (50-500 nm physical diameter at 50 % counting efficiency, extending to 20 and 700 nm with counting efficiency decreasing to 0) aerosol mass composition at 1 Hz resolution. Particles were sampled in-situ through a dedicated inlet (HIMIL⁵⁰) and aerodynamic lens into a vacuum chamber, flash vapourized at 600 °C and analyzed by electron impact time-of-flight mass spectrometry. Overall instrument sensitivity was calibrated every flight day, and sulfate relative ionization efficiencies and instrument particle transmission at regular intervals during the missions. For improved sensitivity, the raw mass spectra were averaged and analyzed at 46 s intervals (about 300 m vertical resolution). Detection limits (as established by periodic blanks) for organic aerosol and sulfate at that time resolution were on average 75 ng m^{-3} and 10 ng m^{-3} at STP, respectively, and improve by the square root of the number of data-points with further averaging.

Descriptions of models.

Four chemical-transport models were used to compare with the ATom data: GEOS-Chem, with aerosol microphysics from either TOMAS⁵¹ or APM^{27,52}; CAM5 with aerosol microphysics from APM (Luo and Yu, Manuscript in preparation); and CESM with aerosol microphysics from CARMA⁵³⁻⁵⁵. We matched the location and time of the model outputs to our aircraft measurements. Details are given in ED Table 1.

For analyses where biomass burning and dust plumes were filtered from the ATom data, they were likewise filtered from the model outputs using the following methods. For CESM-CARMA, a separate model run was completed with biomass burning switched off, and times when the total mass of dust aerosol exceeding $5 \times 10^{-13} \text{ kg m}^{-3}$ (STP) were removed. For CAM5-APM and GEOS-Chem-APM, times where the number fraction of dust or black carbon particles exceeded 10% and 40% were removed. For GEOS-Chem-TOMAS times where the number fraction of dust and elemental carbon submicron particles exceeded 0.5% were removed.

Sensitivity Studies.

To investigate the causes of model underprediction of CCN from tropical upper tropospheric NPF, we performed model sensitivity studies. CAM5-APM was excluded from this analysis because it is the only model in this study where aerosols are fully coupled to convective clouds and precipitation, which increases run-to-run variability, making it difficult to assess the impact of prescribed changes to the model. In the first study, the nucleation rate between 28°N and 28°S at altitudes above 600 hPa pressure level was increased by a factor of 10. In the second study, oceanic emissions of dimethyl sulfide (DMS) were increased by a factor of 3 globally. DMS contributes to atmospheric SO₂ and is thus a source of condensable inorganic material for forming and growing particles. In the third study, rainout and washout in cloud anvils and large-scale cloud systems, and aqueous oxidation of SO₂ were reduced by a factor of 10 at all altitude between 28°N and 28°S. This is a proxy for reducing cloud processing of particles and gases in descending air, and indicates the potential effect of reducing the physically incorrect representation of sub-grid cloud processing discussed in the main text. This cloud processing scaling is not applied to CESM-CARMA, which is not affected by sub-grid cloud over-processing.

Aerosol Indirect Effects.

We used GEOS-Chem with TOMAS and APM, to estimate the magnitude of the aerosol first indirect effect resulting from tropical upper tropospheric NPF following the method from Kodros and Pierce 2017⁵⁶. For the month of August 2016 (ATom 1), for the base case, and the case with reduced cloud processing of descending air in the tropics, nucleation was switched off at pressures < 600 hPa between 28 °N and 28 °S. This caused a change in magnitude of the globally averaged aerosol first indirect effect (ED Fig.10), which was -0.12 and -0.14 W m⁻² for GEOS-Chem-TOMAS, and -0.039 and -0.031 W m⁻² for GEOS-Chem-APM for the base and reduced cloud processing cases, respectively. GEOS-Chem-APM shows a positive radiative forcing in regions where liquid water content in the upper troposphere is elevated. High liquid water content indicates stronger vertical transport, and therefore more particles will be lofted from the lower troposphere in these regions. Turning off nucleation here therefore reduces the number of particles competing for the available condensable vapours, so more vapours condense onto lofted

particles, growing them to sizes where they can act as CCN. This increases the cloud drop number and thus the cloud optical depth. For GEOS-Chem-TOMAS, we ran the same calculation for each month of the year (starting August 2016), and noticed a seasonal cycle (ED Fig. 10), which is likely due to the seasonally dependent position of the ITCZ shifting the fraction of the tropics that contain pollution emitted in the northern hemisphere. Discrepancies between the models and observations exist, and we have only considered the first aerosol indirect effect, therefore these calculations are only an estimate of the magnitude of the radiative effect of tropically upper tropospheric NPF.

References

- 31 Brock, C. A. *et al.* Aerosol size distributions during the Atmospheric Tomography Mission (ATom): methods, uncertainties, and data products. *Atmos Meas Tech* **12**, 3081-3099, doi:10.5194/amt-12-3081-2019 (2019).
- 32 Williamson, C. *et al.* Fast time response measurements of particle size distributions in the 3-60 nm size range with the nucleation mode aerosol size spectrometer. *Atmos. Meas. Tech.* **11**, 3491-3509, doi:10.5194/amt-11-3491-2018 (2018).
- 33 Brock, C. A. *et al.* Sources of particulate matter in the northeastern United States in summer: 2. Evolution of chemical and microphysical properties. *J. Geophys. Res. Atmos.* **113** (2008).
- 34 Brock, C. A. *et al.* Ultrafine particle size distributions measured in aircraft exhaust plumes. *J. Geophys. Res. Atmos.* **105**, 26555-26567, doi:Doi 10.1029/2000jd900360 (2000).
- 35 Kupc, A., Williamson, C., Wagner, N. L., Richardson, M. & Brock, C. A. Modification, calibration, and performance of the Ultra-High Sensitivity Aerosol Spectrometer for particle size distribution and volatility measurements during the Atmospheric Tomography Mission (ATom) airborne campaign. *Atmos. Meas. Tech.* **11**, 369-383, doi:10.5194/amt-11-369-2018 (2018).
- 36 Cai, Y., Montague, D. C., Mooiweer-Bryan, W. & Deshler, T. Performance characteristics of the ultra high sensitivity aerosol spectrometer for particles between 55 and 800 nm: Laboratory and field studies. *J. Aerosol Sci.* **39**, 759-769, doi:10.1016/j.jaerosci.2008.04.007 (2008).
- 37 Murphy, D. M. Time offsets and power spectra of the ER-2 data set from the 1987 airborne antarctic ozone experiment. *J. Geophys. Res. Atmos.* **94**, 16737-16748, doi:DOI 10.1029/JD094iD14p16737 (1989).
- 38 Weber, R. J. *et al.* Spurious aerosol measurements when sampling from aircraft in the vicinity of clouds. *J. Geophys. Res. Atmos. s* **103**, 28337-28346, doi:Doi 10.1029/98jd02086 (1998).
- 39 Seinfeld, J. H. & Pandis, S. N. *Atmospheric Chemistry and Physics: From Air Pollution to Climate Change, 1st edition.* (Wiley, New York, NY, USA, 1998).
- 40 Lovejoy, E. R., Curtius, J. & Froyd, K. D. Atmospheric ion-induced nucleation of sulfuric acid and water. *J. Geophys. Res. Atmos.* **109**, doi:Artn D08204 10.1029/2003jd004460 (2004).
- 41 Kim, S. *et al.* PubChem Substance and Compound databases. *Nucleic Acids Res.* **44**, D1202-D1213, doi:10.1093/nar/gkv951 (2016).

- 42 Westervelt, D. M. *et al.* Formation and growth of nucleated particles into cloud condensation nuclei: model-measurement comparison. *Atmos Chem Phys* **13**, 7645-7663 (2013).
- 43 Bowman, K. P. Large-scale isentropic mixing properties of the Antarctic polar vortex from analyzed winds. *J. Geophys. Res. Atmos.* **98**, 23013-23027, doi:Doi 10.1029/93jd02599 (1993).
- 44 National Centers for Environmental Prediction, National Weather Service, NOAA, U.S. Department of Commerce. *NCEP GFS 0.25-degree global forecast grids historical archive*. Research Data Archive at the National Center for Atmospheric Research, Computational and Information Systems Laboratory. Doi.org/10.5065/D65D8PWK. Accessed 28 May 2018 (2015, updated daily).
- 45 NASA Langley Cloud and Radiation Research Group, Satellite imagery and cloud products page, www.cloudsway2.larc.nasa.gov, (Accessed 28 May 2018).
- 46 Murphy, D. M. *et al.* Single-particle mass spectrometry of tropospheric aerosol particles. *J. Geophys. Res. Atmos.* **111**, doi:10.1029/2006jd007340 (2006).
- 47 DeCarlo, P. F. *et al.* Field-deployable, high-resolution, time-of-flight aerosol mass spectrometer. *Anal. Chem.* **78**, 8281-8289, doi:10.1021/ac061249n (2006).
- 48 Canagaratna, M. R. *et al.* Chemical and microphysical characterization of ambient aerosols with the Aerodyne Aerosol Mass Spectrometer. *Mass Spectrom. Rev.* **26**, 185-222, doi:10.1002/mas.20115 (2007).
- 49 Schroder, J. C. *et al.* Sources and secondary production of organic aerosols in the northeastern United States during WINTER. *J. Geophys. Res. Atmos.* **123**, 7771-7796, doi:10.1029/2018jd028475 (2018).
- 50 Stith, J. L. *et al.* An overview of aircraft observations from the Pacific Dust Experiment campaign. *J. Geophys. Res. Atmos.* **114**, doi:Artn D05207 10.1029/2008jd010924 (2009).
- 51 Kodros, J. K., Cucinotta, R., Ridley, D. A., Wiedinmyer, C. & Pierce, J. R. The aerosol radiative effects of uncontrolled combustion of domestic waste. *Atmos. Chem. Phys.* **16**, 6771-6784, doi:10.5194/acp-16-6771-2016 (2016).
- 52 Yu, F. & Luo, G. Simulation of particle size distribution with a global aerosol model: Contribution of nucleation to aerosol and CCN number concentrations. *Atmos. Chem. Phys.* **9**, 7691-7710 (2009).
- 53 Toon, O. B., Turco, R. P., Westphal, D., Malone, R. & Liu, M. S. A multidimensional model for aerosols - Description of computational analogs. *J. Atmos. Sci.* **45**, 2123-2143, doi:Doi 10.1175/1520-0469 (1988).
- 54 Yu, P. *et al.* Evaluations of tropospheric aerosol properties simulated by the community earth system model with a sectional aerosol microphysics scheme. *J. Adv. Model Earth Sy.* **7**, 865-914, doi:10.1002/2014ms000421 (2015).
- 55 Yu, P., et al. Efficient in-cloud removal of aerosols by deep convection. *Geophys. Res. Lett.*, 46. <https://doi.org/10.1029/2018GL080544> (2019).
- 56 Kodros, J. K., Pierce, J. R.: Important global and regional differences in cloud-albedo aerosol indirect effect estimates between simulations with and without prognostic aerosol microphysics, *J. Geophys. Res.*, 122, doi:10.1002/2016JD025886 (2017).
- 57 Williamson, C. J. *et al.* ATom: Tropical New Particle Formation Measurements and Global-Model Outputs, ORNL DAAC, Oak Ridge, Tennessee, USA. <https://doi.org/10.3334/ORNLDAAC/1684> (2019).

- 58 NCAR/UCAR Community Earth System Model CESM1.0 public release page, <http://www.cesm.ucar.edu/models/cesm1.0/>, (Accessed 19 February 2019).
- 59 GEOS-Chem Online User's Guide, <http://acmg.seas.harvard.edu/geos/doc/man/>, (Accessed 19 February 2019).

Data availability.

The full ATom dataset is publicly available¹⁵, as are data specific to this analysis⁵⁷.

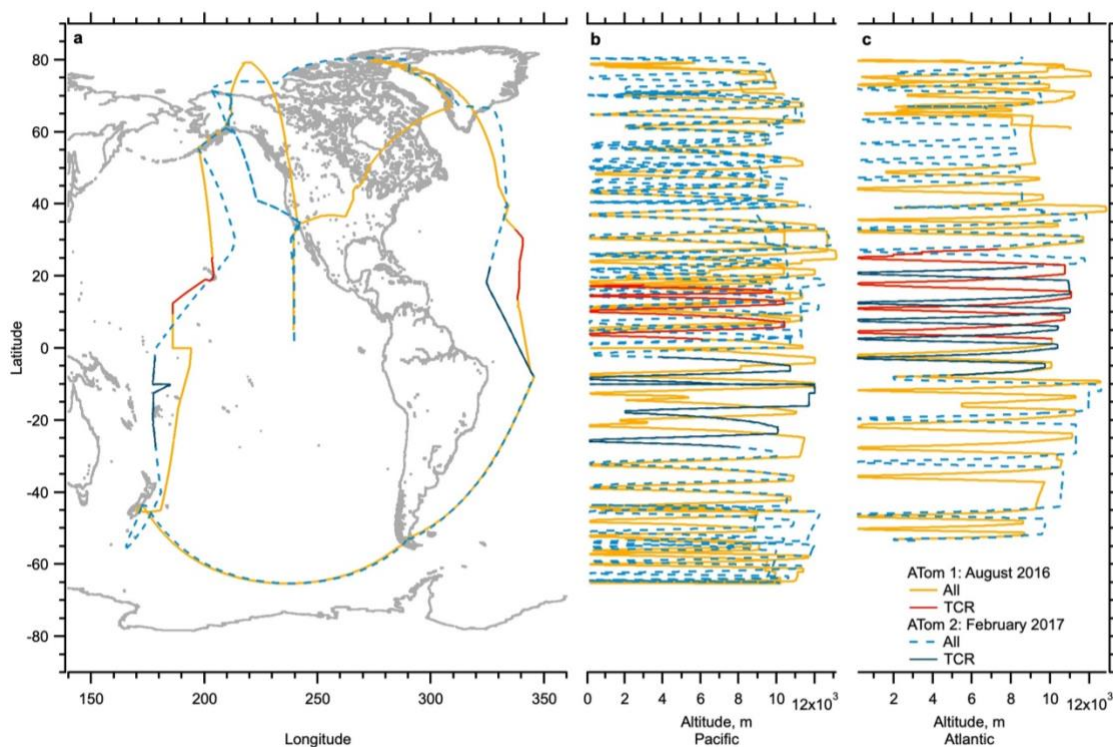
Code availability.

Code for the model CESM with the base version of CARMA is available online⁵⁸, as is code for GEOS-Chem with TOMAS and APM⁵⁹. Code used to analyze ATom data and model output, and recent modifications to CARMA, GEOS-Chem and CAM5 with APM used in this analysis are available on request.

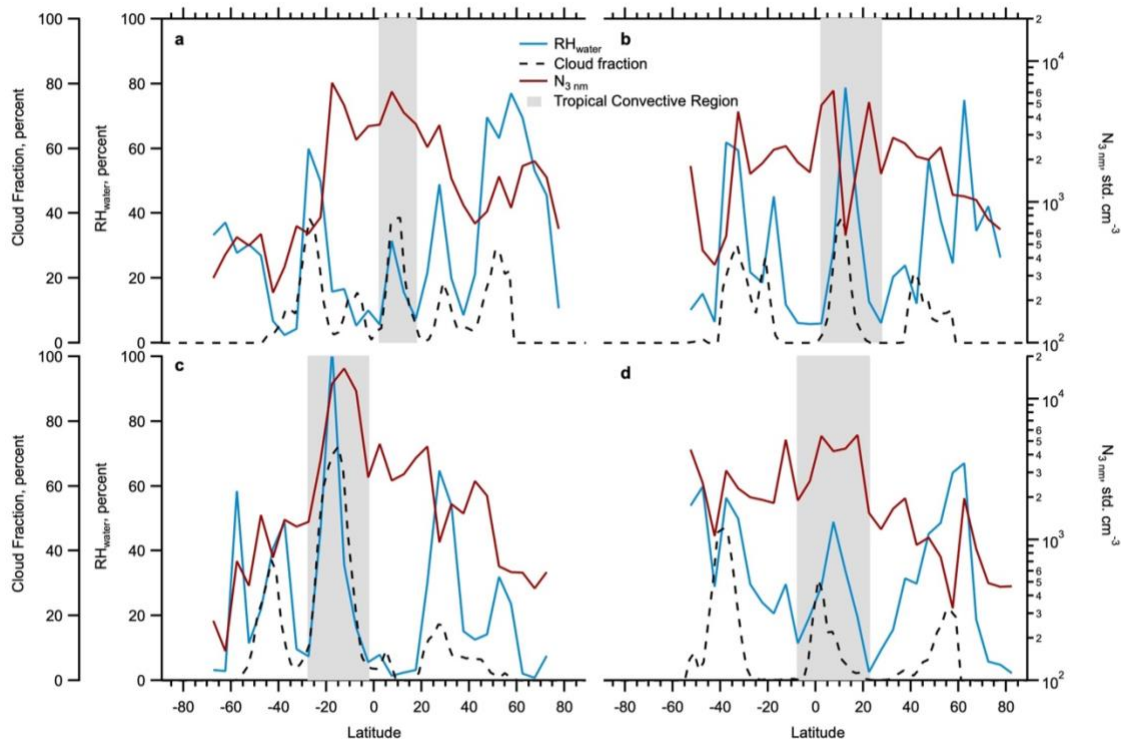
Extended Data

	Geos-Chem-TOMAS	Geos-Chem-APM	Cam5-APM	CESM-CARMA
Meteorology	GEOSFP	MERRA2	Nudging with MERRA2	GEOS5
Horizontal Resolution	4x5	2x2.5	1.9x2.5	1.9x2.5
Vertical Resolution	47 levels	47 levels	32 levels	56 levels
Nucleation Theory	Ternary and binary neutral	Ternary neutral and ternary ion-induced	Ternary neutral and ternary ion-induced	Binary neutral
Condensing Gases	H ₂ SO ₄ , secondary organic vapors*	H ₂ SO ₄ , low volatility secondary organic gases	H ₂ SO ₄ , low volatility secondary organic gases	H ₂ SO ₄ , low volatility secondary organic gases
Size Bins (3-60 nm)	7	19	19	7
Size Bins (> 60 nm)	8	15	15	13
Mixing State	Internal	Semi-external	Semi-external	Semi-external

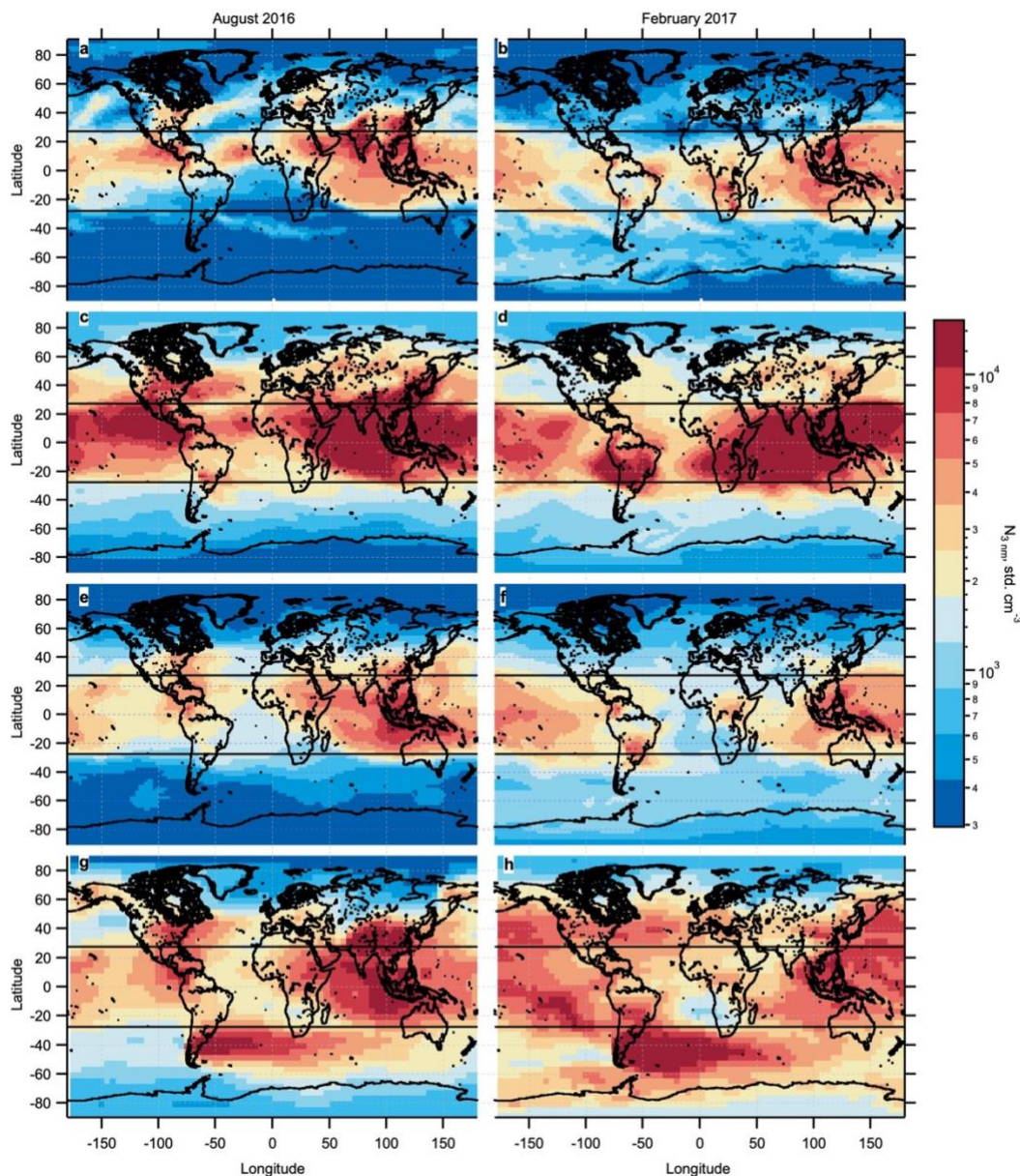
Extended Data Table 1| Relevant properties of the models. * organics formed in boundary layer only



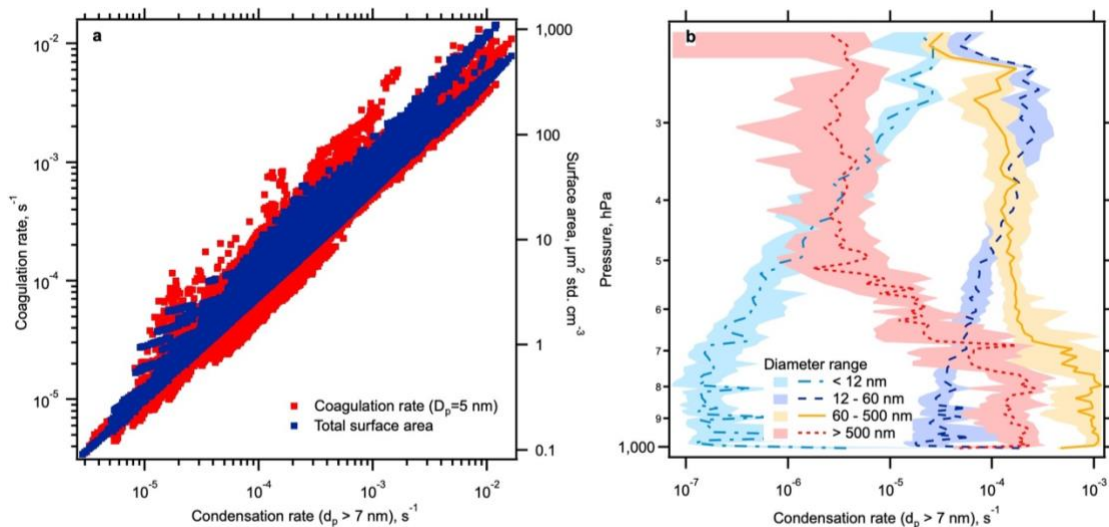
Extended Data Figure 1| Location of ATom measurements. a, ATom 1 (gold) and 2 (blue) measurements by latitude and longitude. b, c, Altitude and latitude of measurements over the Pacific and Atlantic respectively. Tropical convective regions (TCRs) are highlighted in red (ATom 1) and dark blue (ATom 2).



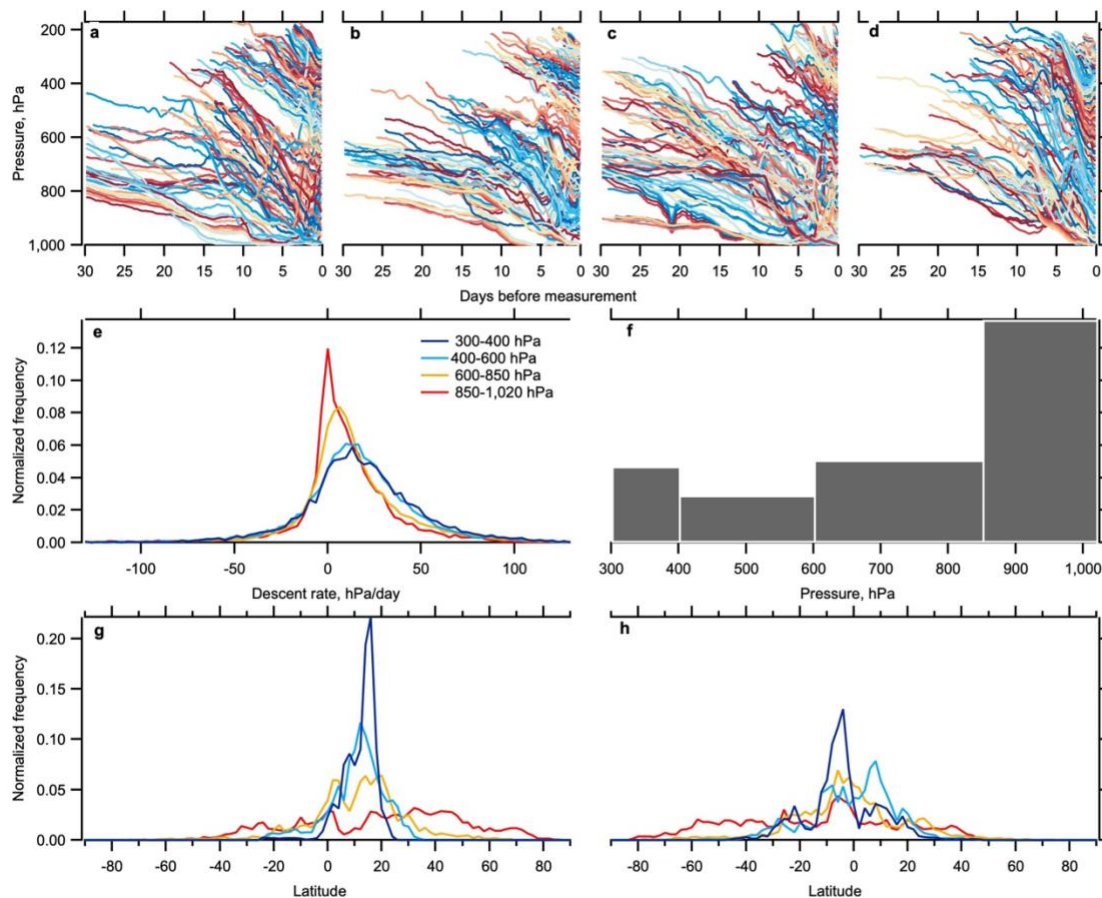
Extended Data Figure 2 | Identifying the tropical convective region. Average measured RH over water (blue), number concentration of particles ≥ 3 nm (red), and cloud fraction from reanalysis meteorology (dashed black) between 200 and 400 hPa. **a, b**, ATom 1 Pacific and Atlantic transects, **c, d**, ATom 2 Pacific and Atlantic transects. We take the central peak in RH to be the Inter Tropical Convergence Zone (ITCZ), and define a tropical convective region (TCR) between the minima on either side of this peak (grey shaded). These correspond to latitudes 2.5 to 17.5 °N ATom 1 Pacific, 2.5 to 27.5 °N ATom 1 Atlantic, 27.5 °S to 2.5 °S ATom 2 Pacific, and 7.5 °S to 22.5 °N ATom 2 Atlantic.



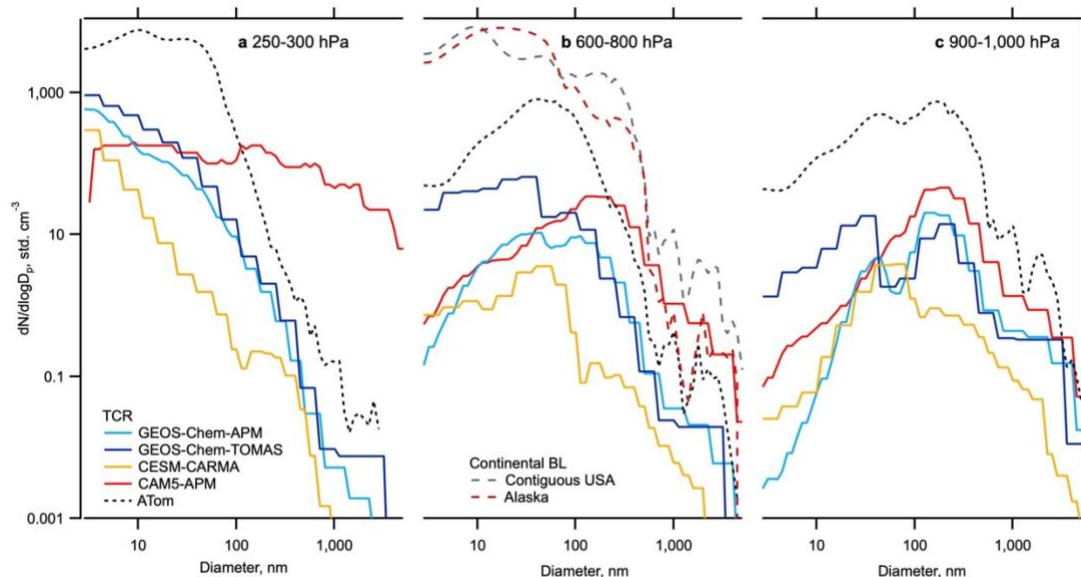
Extended Data Figure 3 | Modeled global concentrations of particles >3 nm. Monthly mean number concentration of particles >3 nm (N_3) in the free troposphere at pressures less than 600 hPa (weighted by grid-box height) modeled for August 2016 (left) and February 2017 (right). **a, b**, CESM-CARMA, **c, d**, CAM5-APM, **e, f**, GEOS-Chem-APM, and **g, h**, GEOS-Chem-TOMAS. Horizontal black lines mark the TCR defined by the ATom data. GEOS-Chem-TOMAS (g,h) shows higher number concentrations of N_3 outside the TCR than the other models. This is partly the effect of 2009 volcanic emissions, which are included in the emission database for this model.



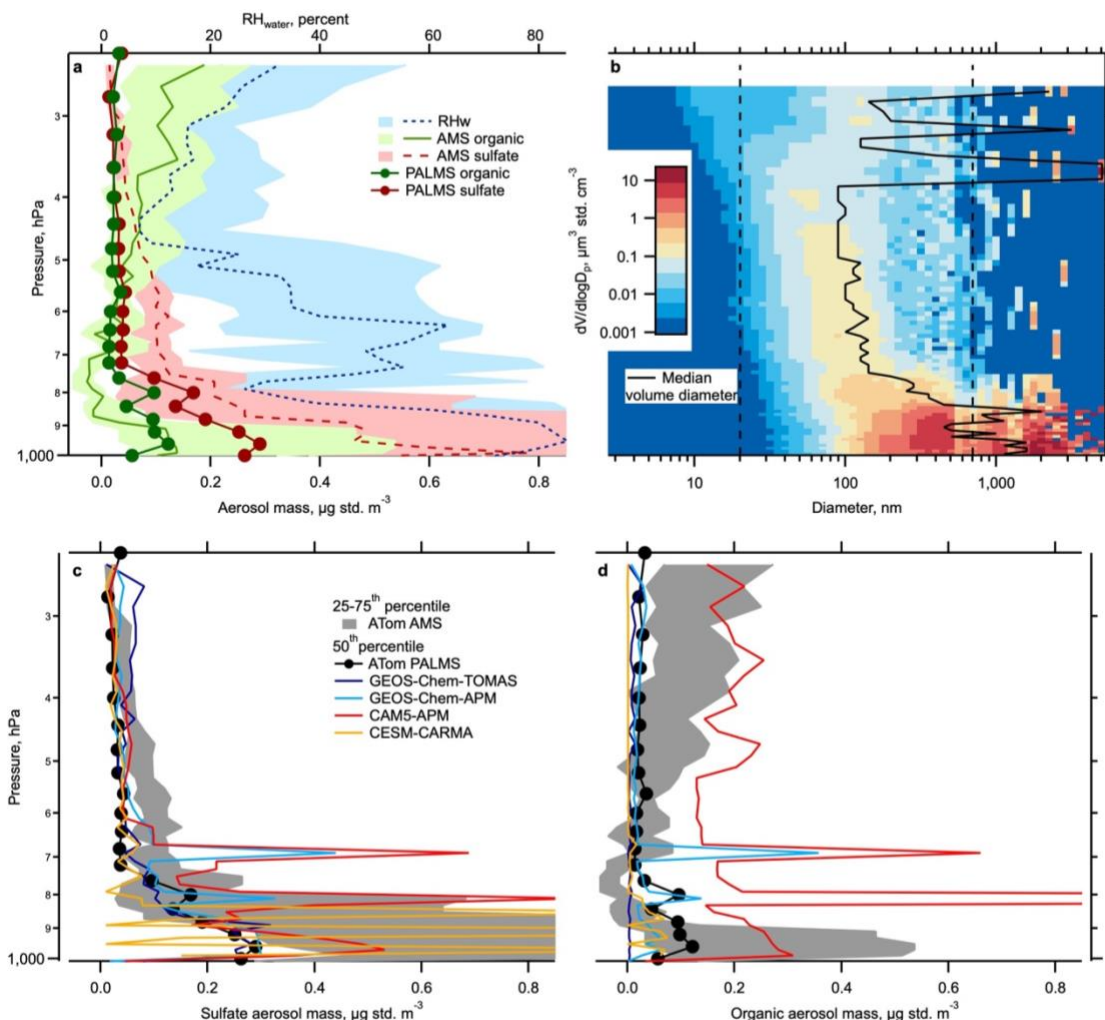
Extended Data Figure 4 | Condensation and coagulation rate details. **a**, The relationship between the gas-phase condensation rate onto particles larger than 7 nm, coagulation rate between 5 nm particles and all other particles, and the total aerosol surface area (2.6-4800 nm), which show a strongly linear relationship. **b**, The contribution of each mode to the average condensation rate in the TCR as a function of pressure. This shows that this sink is not always dominated by particles >60 nm, but that, especially at high altitude, 12-60 nm particles (Aitken mode) can dominate the coagulation sink, and must therefore be considered. Lines are 50th percentile, shaded areas 25-75th percentile range.



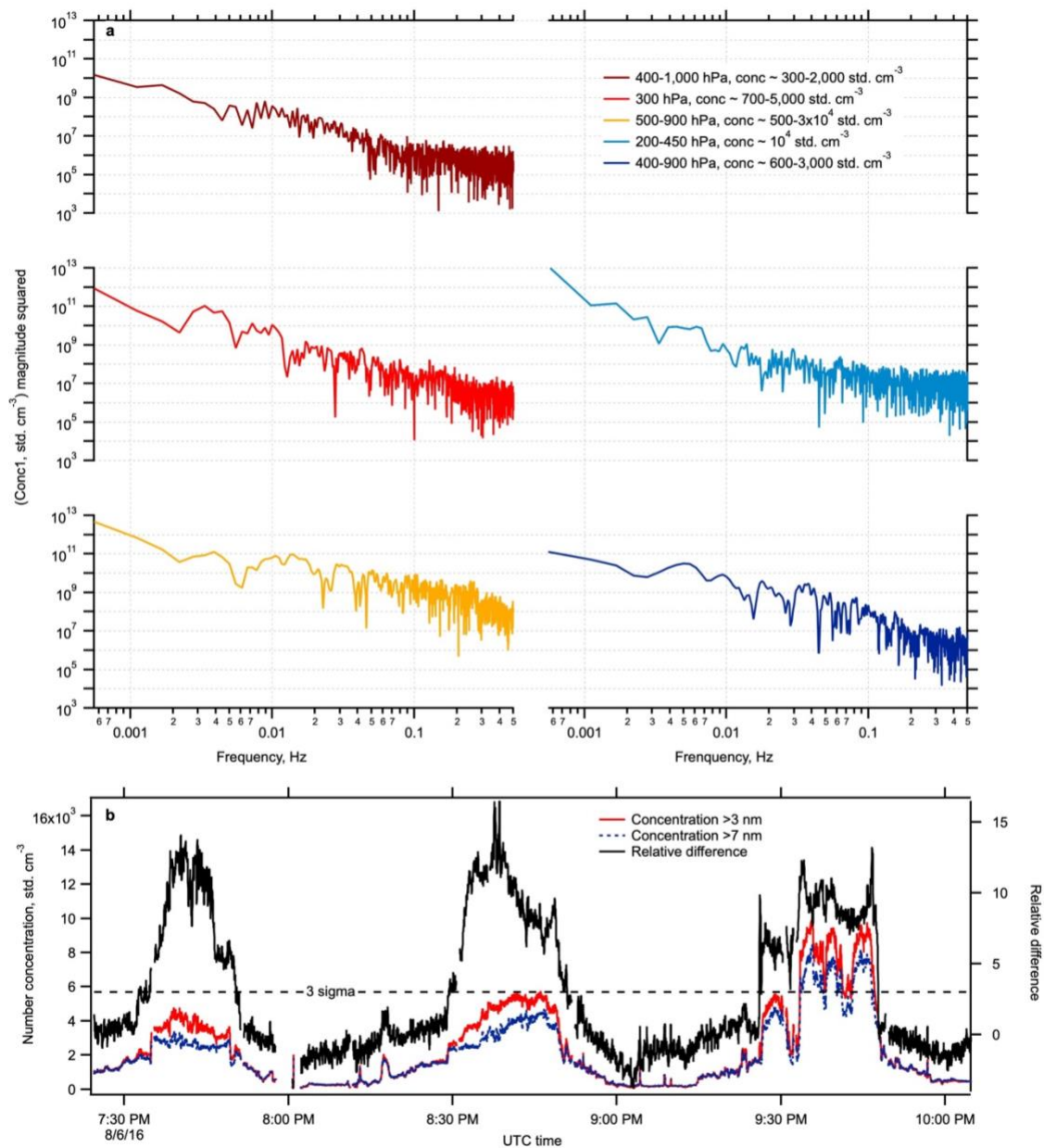
Extended Data Figure 5 | TCR Back-trajectories. 30-day back trajectories calculated every minute of flight time within the TCRs. **a-d**, Pressure from the time of minimum pressure of the trajectory to the flight track for all back trajectories from ATom 1 Pacific and Atlantic and ATom 2 Pacific and Atlantic respectively. Colours distinguish separate trajectories. The general slope of increasing pressure with time indicates a general descending motion of the air. **e**, Histogram of instantaneous descent rates (1 point every 3 hours) of all trajectories within the pressure-bins shown in the legend. The skew at all altitudes towards positive descent rates is evidence of an overall descending motion of the air. The mean descent rate is higher at higher altitudes, and almost 0 at the lowest altitudes, which is to be expected as this is often within the MBL where the air cannot descend further. **f**, Average fraction of time trajectories spent in cloud between the time of minimum pressure and the flight track. In-cloud time was taken as $RH \geq 90\%$ (an overestimate). It is binned by the pressure on the flight track (not the pressure of the trajectory itself as in (e)). For measurements made at pressures <850 hPa, the air spent less than 5% of its time in cloud on average. For air at pressures >850 hPa this increased to $\sim 14\%$. This shows that most of the particles descend with the air instead of being removed by clouds. **g, h**, Histograms of the latitudes of the trajectories between the minimum pressure and flight-track for ATom 1 and 2 respectively, coloured by pressure of the point on the flight-track. Apart from at the lowest altitudes, air parcels entering the flight track mostly remain within the tropics (histograms peak around the equator). Peaks shift towards the summer hemisphere with the season, in the same manner as the TCRs.



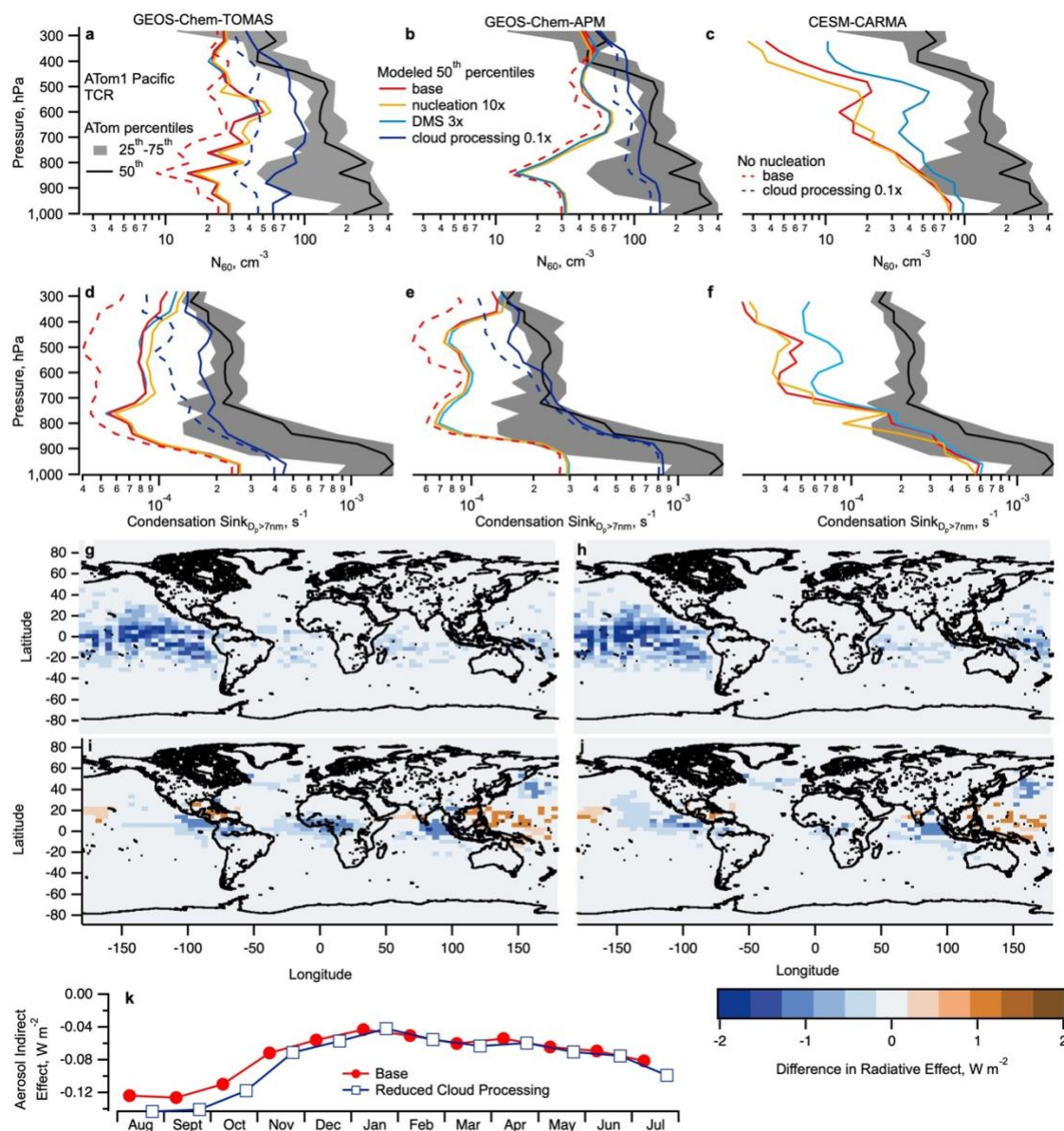
Extended Data Figure 6 | Average Size Distributions. **a, b, c,** Average size distributions in the tropical convective regions between 250 and 300 hPa, 600 and 800 hPa, and 800 and 1000 hPa respectively. Regions of biomass burning or dust plumes have been excluded. Except for particles >100 nm in CAM5-APM, the models show fewer particles than the observations. All models except for CAM5-APM show strong evidence of cloud processing in the form of the dip in the size distribution around 60-100 nm in panels (b) and (c). This indication of cloud processing²³ is far less pronounced in the ATom data, suggesting that too many particles are being cloud processed in the models. (b) also shows average size distributions measured between 900-1000 hPa over the contiguous USA and Alaska, as examples of continental size distributions.



Extended Data Figure 7 | Chemical composition of particles in the TCR. **a**, Organic and sulfate mass of particles, measured by the AMS (50-500 nm) and PALMS (150-500 nm), and ambient RH for the TCR with data affected by biomass burning and dust plumes removed (AMS excludes ATom 2 Pacific where overall mass was too low to measure sulfate and organic components). Both composition measurements have limitations in this regime (the AMS is close to detection limit, and PALMS cannot measure particles <150 nm), so perfect agreement is not expected. However, low sulfate mass at high altitude seems robust as it is supported by both measurements, and differences between PALMS and AMS organic concentrations suggest organics dominate smaller particle composition at high altitude. **b**, Size resolved volume in the TCR. Between 400 and 800 hPa the median diameter by volume, and the majority of the aerosol volume, is within the measured 50-500 nm range. The composition results should thus be regarded as informative within this pressure range. **c**, **d**, Modeled sulfate and organic masses over the same regions compared with measurements.



Extended Data Figure 8 | Details from NMASS data. a, Identifying instrumental noise on particle measurements using Fourier transforms of number concentration of particles >3 nm as measured in the first NMASS channel, for 30 minutes of data at different altitudes and total concentrations. **b**, Concentrations from the 1st and 2nd channels of NMASS 1 (red and blue respectively), and the calculated relative difference (black) for an example time period. Missing data are when the aircraft flew through a cloud and the data were discarded. Three standard deviations (sigma) relative difference is shown in the dashed horizontal line. Any relative difference larger than this is considered statistically significant.



Extended Data Figure 9 | Sensitivity studies and radiative effects. Changes to modeled N_{60} and condensation sink for ATom 1 Pacific for GEOS-Chem-TOMAS (a,d), -APM (b,e) and CESM-CARMA (c,f), with the base model run (red), nucleation rates increased by a factor of 10 between 28 °N and 28 °S at pressures < 600 hPa (orange), oceanic emissions of DMS tripled (light blue), cloud processing on descent reduced by a factor of 10 (dark blue), and nucleation turned off between 28 °N and 28 °S at pressures < 600 hPa (dashed). These results are compared to the ATom observations (black and grey). Simulated aerosol indirect effect from tropical upper tropospheric NPF (g,h GEOS-Chem-TOMAS; i, j GEOS-Chem-APM) for the base and reduced cloud processing cases respectively, calculated by turning off nucleation 28 °N-28 °S at pressures below 600 hPa. The seasonal cycle of this global aerosol indirect effect for GEOS-Chem-TOMAS (k) for the base (red) and reduced cloud processing (blue) case.